# Application and performance study of protective coatings in corrosion resistance on industrial equipment surfaces



Jing Wang<sup>1</sup>

<sup>1</sup>College of Chemistry and Chemical Engineering, Shandong University, Jinan, Shandong, 250101, China

\*Corresponding Author: w\_jing11096@193.com

Received: 16/05/2025 Revised: 29/07/2025 Accepted: 23/08/2025 Published: 26/10/2025

©2025 The Author(s). This is an open access article under the CC BY license https://creativecommons.org/licenses/by/4.0/

Abstract: Corrosive environments cause severe damage to industrial equipment, potentially leading to corrosion of components, leakage of corrosive media, and even safety incidents. This study investigates protective coatings for cemented carbide cutting tools in industrial equipment. A gradient TiSiCN coating was deposited on high-speed steel surfaces using multi-arc ion plating. The microstructure and corrosion resistance of the composite TiSiCN coating under varying gas flow ratios were evaluated using X-ray diffraction (XRD), X-ray photoelectron spectroscopy (XPS), nanoindentation testing, high-temperature friction and wear experiments, and an electrochemical workstation. Results indicate that the gradient TiSiCN coating primarily consists of TiC and TiCN phases, exhibiting preferred orientation on the TiCN (111) crystal plane. At a 5:5 gas flow ratio, the coating sample achieved a polarization resistance of  $2.297 \times 10^5 \ \Omega \cdot \text{cm}^2$ , surpassing other ratios or single-layer TiSiCN coatings, demonstrating superior corrosion resistance. Therefore, when applying protective coatings to industrial equipment surfaces, it is essential to thoroughly understand both the coating materials and the coating process to effectively ensure the corrosion resistance of the equipment

**Keywords:** multi-arc ion plating, TiSiCN coating, corrosion resistance, gas flow ratio, microstructure

## 1 | Introduction

In modern society, metallic materials are extensively utilized in every aspect of daily life, such as automobiles, bridges, buildings, and various industrial equipment [1, 2]. Corrosion of metallic materials represents one of the most prevalent forms of failure, inflicting substantial economic losses across industries and even causing severe casualties [3]. The corrosion protection provided by coatings for metallic substrates primarily operates through three mechanisms [4, 5, 6]:

The first is physical shielding, where the coating blocks environmental contaminants from reaching the substrate surface, thereby protecting it. This mechanism also underpins the corrosion resistance of paint coatings. The second is corrosion inhibition, achieved by adding a certain amount of corrosion inhibitor to the metal substrate's surroundings or directly into the coating. This reduces the corrosion rate, ultimately providing corrosion resistance. The third mechanism is the cathodic protection provided by the metallic coating,

which is the primary corrosion resistance mechanism for metallic coatings. When corrosive media in the air diffuse into the metallic coating, redox reactions occur between the coating and the substrate. The metallic coating acts as an anode, undergoing oxidation and losing electrons, while the electrons induce a reduction reaction on the substrate, thereby providing cathodic protection.

The anti-corrosion performance of protective coatings has been extensively studied by scholars, yielding satisfactory results over the past 30 years. First, micro-arc oxidation (MAO) has garnered significant attention due to its ability to produce porous, adherent, and bioactive implant coatings [7]. Qi et al. [8] prepared a self-sealing micro-arc oxidation MAO/ZrO<sub>2</sub> composite coating. The incorporation of ZrO<sub>2</sub> particles enhanced the density and surface roughness of the MAO coating structure. The sealed pores significantly reduced the permeability of the corrosive solution, thereby improving the electrochemical corrosion resistance of the coating. Chen et al. [9] applied a  $20\mu$ m ceramic oxide coating via micro-arc oxidation on AZ31 magnesium alloy. This coating protected the substrate from corrosion in 3.5wt% NaCl solution while achieving a microhardness of 410HV—significantly higher than the base material. Wei, Yan and Tian [10] similarly employed micro-arc oxidation to protect aluminum-copper-magnesium alloys with ceramic coatings. A  $100\mu$ m polished coating reduced the friction coefficient and wear rate under oil lubrication to one-tenth and one-thousandth of those under dry sliding conditions. This improvement stems from the micro-arc oxidation film's porous outer zone and dense inner zone, which synergistically enhance the alloy's wear resistance and corrosion resistance.

Organic coatings represent the most widely used method for protecting metal materials against corrosion, particularly crucial in transportation and infrastructure [11]. Polyaniline is a typical conductive polymer. Rout et al. [12] formulated a coating using polyaniline powder as pigment and compared the corrosion resistance of polyaniline-coated steel with bare steel. The corrosion resistance of polyaniline-coated steel in a 3.5% NaCl solution was 10-15 times that of bare steel, with a significant reduction in current density. One et al. [13] employed tetraethoxysilane and polymers as raw materials, depositing them via dip-coating onto stainless steel, galvanized steel, and aluminum alloys. Thermal treatment formed protective coatings on the surfaces. The silicon-polymer hybrid film coating effectively enhanced the corrosion resistance and hardness of the alloy materials. Díaz et al. [14] compared the corrosion resistance of single-layer epoxy-siloxane coatings versus traditional dual-layer epoxy/polyurethane coatings through long-term outdoor testing and accelerated corrosion tests. Results showed the epoxy-siloxane composite film exhibits lower oxygen and water vapor permeability, significantly outperforming conventional coatings in corrosion resistance tests. The addition of a zinc-rich primer further enhances its protective performance. Wang and Cai [15] employed pre-dispersed reduced graphene oxide to modify and optimize epoxy primer and polyurethane coatings, investigating their corrosion-resistant mechanisms. At a graphene content of 0.4%, the epoxy coating exhibited significantly reduced porosity, relatively maximum self-corrosion voltage, and minimum self-corrosion current density. At this point, the low-frequency impedance modulus reached its peak, enhancing the coating's corrosion resistance.

Composite coatings, characterized by high hardness and excellent wear and corrosion resistance, exhibit varying mechanisms and effects on material corrosion protection due to their differing compositions [16]. Baghery et al. [17] employed an electrodeposition method to prepare composite coatings with varying TiO<sub>2</sub> nano-content. Corrosion resistance was tested in 0.5M NaCl, 1M NaOH, and 1M HNO<sub>3</sub> solutions. The study revealed that increasing TiO<sub>2</sub> content enhanced the coating's strength, wear resistance, and corrosion protection. Eremin et al. [18] prepared plasma-based corrosion-resistant and wear-resistant coatings using composite materials. The resulting coatings exhibited a regular cellular structure. Coating 1 demonstrated a corrosion rate of approximately 0.02 mm/year in 53 wt.% sulfuric acid, while Coating 2 exhibited a corrosion rate below 0.01 mm/year, indicating excellent corrosion resistance. Wu et al. [19] developed a three-layer

protective coating using diamond-like carbon, aluminum nitride, and aluminum materials, which was applied to the surface of AZ31 magnesium alloy. The coated AZ31 magnesium alloy exhibited increased surface hardness, reduced friction coefficient, and a corrosion current density reduced to  $1.28 \times 10^{-6}$  A/cm<sup>2</sup> in a 3.5 wt.% NaCl solution. Aal [20] co-deposited Ni-TiO<sub>2</sub> composite coatings on aluminum alloy surfaces. X-ray diffraction and energy-dispersive X-ray spectroscopy evaluated the hardness, corrosion resistance, and wear resistance of pure Ni and Ni-TiO<sub>2</sub> composite coatings. Observations and measurements revealed uniform distribution of TiO<sub>2</sub> molecules within the Ni matrix, enhancing overall performance. Li et al. [21] incorporated nickel ions into CrN coatings and analyzed the effect of nickel ions on the surface structure of CrN coatings via X-ray diffraction. Furthermore, nickel ion implantation into CrN coatings significantly improved the corrosion resistance of the alloy. In protective coating performance testing [22], incorporating inorganic layered  $\alpha$ -zirconium phosphate and organic phenylphosphonic acid zirconium maximally enhanced the wear resistance and corrosion resistance of Ni-W coatings. The composite coating exhibited a corrosion potential of -0.28 V and a corrosion current density of  $2.3 \mu$ A cm<sup>-2</sup> in a 3.5 wt.% NaCl solution, demonstrating excellent corrosion resistance.

Additionally, to enhance the surface properties of aluminum alloy materials, Li and Shi [23] employed laser cladding to fabricate high-entropy alloy coatings based on aluminum with varying molar ratios. Testing revealed that coatings with an aluminum molar ratio of 0.8 exhibited excellent wear resistance and abrasion resistance, making them more suitable as materials for improving aluminum alloy surface properties. Hosking et al. [24] characterized corrosion products on zinc-magnesium coated steel using techniques such as X-ray diffraction. They noted that Mg(OH)<sub>2</sub> on the alloy surface absorbs carbon dioxide to form soluble hydroxycarbonates, enabling insoluble silicate precipitation on the corrosion surface. This protects the alloy interior from readily corroding, thereby enhancing overall corrosion resistance. Amadi and Ukpaka [25] designed corrosion resistance tests for different protective coatings, where fused epoxy resin (FBE) demonstrated superior performance. Adding appropriate corrosion inhibitors effectively delayed material corrosion. Addressing the poor corrosion resistance of carbon steel in marine engineering, Brito, Bastos and Costa [26] evaluated the corrosion resistance of five metal coatings via salt spray and electrochemical polarization tests. Among these, FeCrCo deposition with epoxy sealing demonstrated the best anti-corrosion performance, making it an effective coating for protecting carbon steel in marine environments. As described above, corrosion protection technologies based on protective coatings primarily include micro-arc oxidation coatings, metallic coatings, organic coatings, and chemical conversion coatings [27, 28]. These protective coating technologies not only enhance the corrosion resistance of alloy materials but also improve surface properties such as wear resistance and hydrophobicity. Furthermore, they offer lower costs and simpler operation, leading to their widespread application in the corrosion protection of industrial equipment [29, 30].

In industrial production processes, numerous media exhibit strong corrosive properties, subjecting industrial equipment to extremely severe corrosion challenges. Such corrosion issues significantly increase the likelihood of equipment failures, posing serious threats to production safety and economic efficiency. To address the poor corrosion resistance of industrial equipment surfaces, this study prepared TiSiCN coatings using high-speed steel and silicon wafers. Samples with varying gas flow rates and single-layer coatings were created for comparative analysis to identify the optimal corrosion-resistant protective coating. The TiSiCN coatings were characterized in terms of phase structure, mechanical properties, wear and friction performance, and corrosion resistance. Recommendations are provided for applying protective coatings to industrial equipment surfaces.

## 2 Test materials and characterization methods

The economic demand for higher cutting speeds and feed rates in modern machining, coupled with environmental requirements to reduce the use of harmful coolants and lubricants, has driven significant transformation in the tooling industry. Traditional uncoated cemented carbide tools are gradually being replaced by coated cemented carbide tools. This paper proposes a protective coating material based on TiSiCN, aiming to further enhance the wear and corrosion resistance of alloy tools, thereby better ensuring safety and efficiency in industrial manufacturing processes.

## 2.1 | Materials and methods for preparing protective coatings

#### 2.1.1 | Protective coating preparation materials

This study employed a multi-arc ion plating method to deposit TiSiCN films on substrates of high-speed steel, stainless steel, and silicon wafers. The high-speed steel used was grade M2 (standard designation W6Mo5Cr4V2), with specimen dimensions of  $\Phi$ 25 mm  $\times$  5 mm. The stainless steel substrate selected was austenitic stainless steel with a smooth surface (standard grade: 1Cr17Mn6Ni5N), with sample dimensions of 25  $\times$  25  $\times$  1 mm. Single-crystal silicon wafers were used as substrates, with sample dimensions of 12 mm  $\times$  12 mm. Deposition employed a 99.99% pure Ti target and a 99.99% pure AlCr target, with working gases consisting of 99.96% Ar, 99.99% N<sub>2</sub>, and tetramethylsilane gas [31].

Film deposition imposes stringent requirements on the substrate surface condition, necessitating pretreatment. First, the high-speed steel surface was sequentially ground using 300#, 500#, 900#, and 1200# wet sandpaper. Finally, it was polished with a  $1.2\mu\mathrm{m}$  diamond-particle polishing agent until the surface roughness fell below  $0.6\mu\mathrm{m}$ . The surface was then cleaned with metal cleaning solution and deionized water. Finally, the specimen was placed in 95% pure alcohol for ultrasonic cleaning for 15 minutes, removed, and dried in an oven for later use. Since silicon wafers and stainless steel surfaces are highly smooth, no polishing treatment was required.

#### 2.1.2 | Coating preparation process design

Based on extensive research, agate grinding jars and balls with high hardness were selected for processing various raw materials. The ball milling jar has a volume of 12L, with approximate dimensions of  $\Phi$ 250×350mm. Three sizes of agate balls ( $\Phi$ 18,  $\Phi$ 10, and  $\Phi$ 6) were selected and combined in a 1:1:1 ratio, with the balls accounting for 40%–50% of the total weight. After proportionately blending the raw materials, they were loaded into the agate vessels. The calculated quantity of agate balls was added, followed by alcohol. The total volume must not exceed two-thirds of the ball mill vessel capacity. The mixture was continuously agitated at 80–120 rpm for 80–100 hours, ultimately achieving the required particle size of  $\leq$ 5  $\mu$ m for the raw materials. Using this method, the prepared nano-scale high-temperature resistant anti-corrosion coating exhibits excellent coverage, corrosion resistance, and high-temperature oxidation resistance. The nano-powder and high-temperature resistant multi-component solid powders achieve good dispersion within the coating [32].

Nanoparticles possess high surface activity and large specific surface areas, making them prone to "growing" into larger agglomerates within inorganic silicate film-forming agents. This process causes them to lose their inherent properties, leading to material performance degradation. Physical dispersion methods are employed

to break down these nano-agglomerates: first, dispersion for 10 minutes using a magnetic oscillator at 2600 r/min, followed by mechanical stirring in an agate jar at 1200 r/min for 20 minutes. Adding  $\Phi 5$  ceramic balls induces strong turbulent flow through their rotational self-impact effect, disaggregating and suspending the nanoparticles. This ensures thorough mixing of nanopowders, solids, and film-forming agents in the coating. After coating, the surface becomes dense and smooth, significantly improving surface quality and resolving dispersion challenges with nanomaterials. The coating preparation process is shown in Figure 1, with specific steps as follows:

- (1) Ball-mill metal oxides, nickel-chromium-aluminum-yttrium powder, and high-temperature-resistant multi-component solid powder separately in agate jars to achieve particle size  $\leq 5\mu$ m.
- (2) Weigh the ground solid powders from step (1) according to the formulation ratio and place them uniformly into a ball milling jar, ensuring the volume does not exceed one-third of the jar's capacity. Add agate balls and alcohol, keeping the total volume below two-thirds of the jar's capacity. Mix thoroughly for 80–100 hours.
- (3) Add nano-titanium dioxide (particle size  $\leq 50$  nm) and potassium silicate solution according to the formulation ratio. Stir thoroughly to ensure uniform dispersion of the nano-materials. The composite coating is now prepared. Allow it to cure for 20–30 minutes before use.

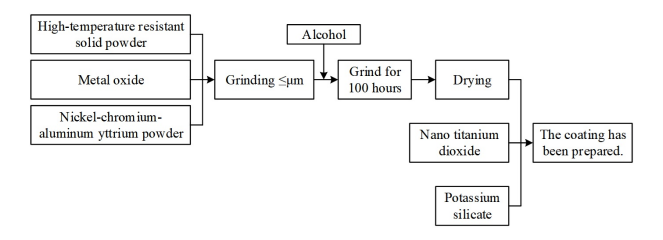


FIGURE 1 The process of preparing coatings

#### 2.1.3 | Protective coating preparation process

Based on the selected coating materials and preparation process, the preparation of the TiSiCN coating proceeds as follows:

First, Ar gas is introduced for ion etching, maintaining an Ar gas flow rate of 100 sccm. During this phase, the target current for the Cr target is controlled at 120 A, with a bias voltage of 220 V. Subsequently, the CrN underlayer preparation begins by switching the gas supply from Ar to N<sub>2</sub>, with the N<sub>2</sub> flow rate controlled at 500 sccm and the vacuum level maintained at 1.2 Pa. After 15 minutes, activate the graphite target for magnetron sputtering to deposit the CrCN transition layer. Maintain an Ar flow rate of 150 sccm, N<sub>2</sub> flow rate of 50 sccm, vacuum level of 0.5 Pa, and graphite target current of 2.5 A. Continue for 15 minutes. Finally, activate the TiSi target to begin depositing the TiSiCN functional coating. Maintain a duty cycle of 40%, with the TiSi target current at 120 A and the graphite target current at 3.0 A for 90 minutes. Ensuring the total flow rate of N<sub>2</sub> and Ar gas was maintained at 240 sccm, the relative proportions of N<sub>2</sub> and Ar gas flow rates were varied to prepare a set of TiSiCN coatings with different N<sub>2</sub>/Ar flow ratios: 2:8, 4:6, and 5:5, designated as coatings EX1–EX3. Additionally, a single-layer TiSiCN coating was prepared as a control group for the multi-layer gradient TiSiCN coatings using the same method as for EX4 coating preparation. This control

group was designated as EX4. The preparation process parameters are shown in Table 1.

-	Bias voltage	Current	$N_2$	Ar	Т	Air pressure	Time
EX1	100V	3.0A	48sccm	192sccm	300℃	0.5Pa	90min
EX2	100V	3.0A	96sccm	144sccm	300℃	0.5Pa	90min
EX3	100V	3.0A	120sccm	120ccm	300℃	0.5Pa	90min
EX4	100V	3.0A	120sccm	120sccm	100°€	0.8Pa	90min

TABLE 1 Process parameters of TiSiCN coating

## 2.2 Methods for characterizing the performance of protective coatings

#### 2.2.1 | Phase structure characterization

- (1) X-ray Diffractometer. A Bruker AXS D8 Advance X-ray diffractometer (XRD) was employed to investigate the crystal structure variations of different coatings with respect to process parameters. The parameters were: scan range 20/80, step size 0.0205/1 (sec), and  $Cu/K\alpha$  wavelength 1.5412 Å.
- (2) X-ray Photoelectron Spectroscopy. XPS identifies elemental composition by determining the binding energy of core levels during photoelectron emission. Different elements correspond to distinct core levels, and energy shifts reflect changes in chemical bonding states. In this study, an AXIS Ultra DLD multifunctional XPS system was employed, utilizing a monochromatized Al  $K\alpha$  radiation source with an energy of 1485.4 eV and a resolution of 0.51 eV. Prior to experiments, Ar ion etching was performed to remove contaminants such as adsorbed substances that could affect experimental results [33].
- (3) Scanning Electron Microscopy (SEM). A S-4800 field emission SEM was used to observe the surface and cross-sectional morphology of samples. Operating parameters included an acceleration voltage of 0.6-35 kV and a magnification range of  $50-90,000\times$ . The instrument was equipped with an energy-dispersive X-ray spectrometer (EDS) for elemental analysis.
- (4) Transmission Electron Microscopy (TEM). A FEI Tecnai F20 TEM was employed with an acceleration voltage of 220 keV and a point resolution of 0.25 nm. TEM specimens were prepared by depositing a 90 nm thick film onto a single-crystal NaCl substrate. After dissolution in deionized water, the film was retrieved using a microgrid for measurement.
- (5) Scanning Probe Microscope. Surface topography and roughness of the coating were analyzed using a Veeco Dimension 3100 V scanning probe microscope. Operating modes include Scanning Tunneling Microscopy and Atomic Force Microscopy. In this study, the atomic force microscopy (AFM) tapping mode within SPM was employed to analyze the surface morphology and roughness of the coating. The scanning rate was set at 1.5 Hz, with a scanning range of 2  $\mu$ m × 2  $\mu$ m.

## 2.2.2 | Coating mechanical properties testing

The hardness and modulus of the coating were tested using a nanoindentation testing instrument. A Berkovich diamond indenter was selected, and measurements were performed using the continuous stiffness measurement (CSM) method. The CSM mode, based on the Oliver and Pharr model, was employed to obtain parameters

corresponding to the load-displacement curve. Prior to testing, the instrument was calibrated and tested on a standard sample (fused quartz) to ensure compliance with instrument specifications. For characterizing the hardness and Young's modulus of TiSiCN coatings using the G200 nanoindentation tester, the indentation depth was set to 1600 nm. For characterizing the hardness of TiSiCN coatings in the as-deposited state and the hardness and modulus of the indented surface after high-temperature friction, the indentation depth was set to 2200 nm. For testing the hardness and modulus of TaN/ZrN coatings in the as-deposited state and on post-high-temperature-friction scratched surfaces, indentation depths were set to 2200 nm and 1600 nm, respectively. To evaluate the fracture strength of TiSiCN coatings, micro-columns were fabricated on the coatings using FIB technology. Fracture strength testing was then performed using nanoindentation. Unlike hardness and modulus testing, a flat indenter was selected for this test.

Coating adhesion was measured using CSM Instruments' Revetest system. Force application employed a linear scratch method with a diamond Rockwell indenter featuring a  $100^{\circ}$  cone angle and  $250\mu m$  radius. Key test parameters included scratch distance and maximum applied force. For TiSiCN coating scratch testing, the scratch length is set to 6 mm, and the maximum load is set to 60 N. The adhesion strength test parameters for TiSiCN coatings are configured as follows: scratch distance 6 mm, scratch speed 1.2 mm/min, initial load 2 N, and maximum load 120 N.

#### 2.2.3 | Coating friction and wear performance testing

This study simulates and characterizes the mechanical properties of coatings under high-temperature conditions through high-temperature friction and wear experiments. A Bruker UMT-Tribolab friction and wear tester was employed, utilizing a rotating module to conduct high-temperature friction and wear tests on the coatings [34]. The wear specimens measured 30 mm  $\times$  30 mm  $\times$  3 mm. Prior to testing, specimens underwent grinding and polishing to achieve a surface roughness of Ra =  $0.25 \pm 0.12~\mu m$ . The friction pair consisted of a  $\Phi 6.5$  mm Al<sub>2</sub>O<sub>3</sub> ball (hardness 1600 HV). Testing conditions included a temperature of 800°C, a load of 20 N, and a rotational speed of 350 r/min. The test duration was 1 hour, with a wear scar radius of 5 mm. After the experiment, the wear debris was collected and analyzed using SEM. Simultaneously, the cross-section of the coating wear scar was measured using a KLA-Tencor Alphastep P-7 probe contact profilometer. The wear volume and wear rate were calculated using the following formulas:

$$V = \pi dS, \tag{1}$$

$$W = V/PL. (2)$$

In the equation, V represents the wear volume, d denotes the diameter of the wear track, S indicates the cross-sectional area of the wear track, W signifies the wear rate, P represents the applied load, and L denotes the wear distance.

#### 2.2.4 | Electrochemical performance testing of coating corrosion

Electrochemical testing of TiSiCN coatings was conducted using a PARSTAT 4100 electrochemical workstation. The testing apparatus comprised an electrochemical potentiostat, a reference electrode, a working electrode,

and a data acquisition system. Platinum (Pt) served as the counter electrode, silver/silver chloride (Ag/AgCl) as the reference electrode, and the TiSiCN-coated specimen as the working electrode. Since the TiSiCN coating itself is conductive, a wire was welded to the uncoated side of the substrate. The coated sample was then cold-embedded using epoxy resin and a curing agent, exposing a circular area of 10 mm diameter for contact with the corrosion solution. Tests were conducted in a 3.6 wt.% NaCl solution at room temperature. Polarization curves of the coated specimens were measured using Tafelplot technology, and the corrosion potential and corrosion current density were determined via Tafel extrapolation. The scan range was -3 V to +3 V, with a scan rate of 2 mV/s.

## 3 | Performance study of protective coatings

Hard films prepared by physical and chemical vapor deposition exhibit outstanding mechanical properties, corrosion resistance, and tribological performance. They enhance the mechanical properties, corrosion resistance, wear resistance, and oxidation resistance of metal materials and their components, finding extensive applications in industrial sectors such as the power industry, geological drilling, aerospace, and mold and cutting tool manufacturing. This chapter focuses on performance testing of TiSiCN coatings, providing a research model for enhancing the corrosion resistance of industrial equipment.

## 3.1 | Microstructure of the coating

#### 3.1.1 | Differences in phase structure of coatings

For the TiSiCN coatings prepared in this study under four different gas flow rates, XRD patterns of the coatings at various gas flow rates were obtained using the phase characterization methods described earlier, as shown in Figure 2. The data indicate that the coating consists of two phases: TiC (PDF 32-1383) with an NaCl (B1-type) FCC structure and TiCN (PDF 42-148) with a B1-type FCC structure. The TiC phase appears at 36.2°, corresponding to the (111) crystal plane, while the TiCN phase appears at 38.4°, 45.1°, 67.2°, and 84.3°, corresponding to the (111), (200), (220), and (222) crystal planes, indicating preferential orientation of the coating along the TiCN (111) plane. At a gas flow ratio of 2:8 (EX1), the migration and nucleation rate of deposited particles on the substrate is low. The TiC phase in the coating is not prominent on the (111) crystal plane, exhibiting broad half-widths of diffraction peaks and fine grain sizes. As the gas flow rate increased, TiC began nucleating and growing on the (111) plane within the coating. The intensities of diffraction peaks for both TiC and TiCN increased across all crystal planes. Concurrently, particles deposited on the substrate gained sufficient energy to migrate, nucleate, and grow. Consequently, the diffraction peaks became sharper, their half-widths decreased, and grain sizes enlarged, indicating excellent crystallinity of the coating at this point.

Calculations reveal that as the gas flow rate increases from low to high, the grain sizes of the coating are 15.14 nm, 21.38 nm, 25.62 nm, and 29.17 nm, respectively. However, the phase identification in the figure shows no phases containing silicon (Si). This is likely because the deposition process readily forms an amorphous  $Si_3N_4$  structure, which cannot be detected by XRD.

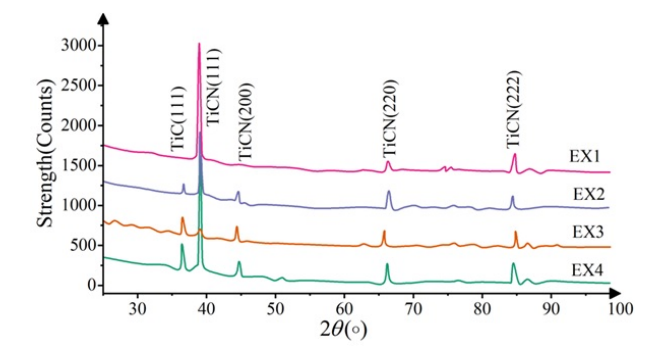


FIGURE 2 XRD patterns of the composite TiSiCN coatings

## 3.1.2 | XPS spectra of elements

Since XRD spectra cannot detect the presence of Si, further analysis of the XPS spectra for elements in the multilayer step coating was conducted based on the XRD patterns, as shown in Figure 3. Specifically, Figure 3(a) and (b) represent the XPS spectra for N and Si elements, respectively. As evident from the figure, the N element exhibits two binding energy peaks at 395.51 eV and 397.25 eV. Given the proximity of Ti-N (395.3 eV) and Al-N (397.4 eV) bonding energies, the 395.51 eV peak indicates the formation of both Ti-N and Si-N bonds in the coating, while the 397.25 eV peak corresponds to the Si-N bond. The XPS energy levels of Si in the multilayer gradient coating reveal binding energies of 97.91 eV and 100.51 eV, corresponding to Ti-Si and Si-N bonds, respectively. However, XRD analysis did not detect Si<sub>3</sub>N<sub>4</sub> diffraction peaks, indicating that Si primarily exists as an amorphous Si<sub>3</sub>N<sub>4</sub> phase within the coating. The XRD diffraction peaks exhibited reduced intensity and broadening. This occurs because the Si<sub>3</sub>N<sub>4</sub> formed by Si incorporation inhibits the growth of the (Ti, Al)N phase, leading to grain refinement, decreased peak intensity, and broadening. The diffraction peaks of the multilayer gradient coating showed lower intensity and more pronounced broadening compared to the monolayer coating, indicating that the multilayer gradient structure also contributes to grain refinement.

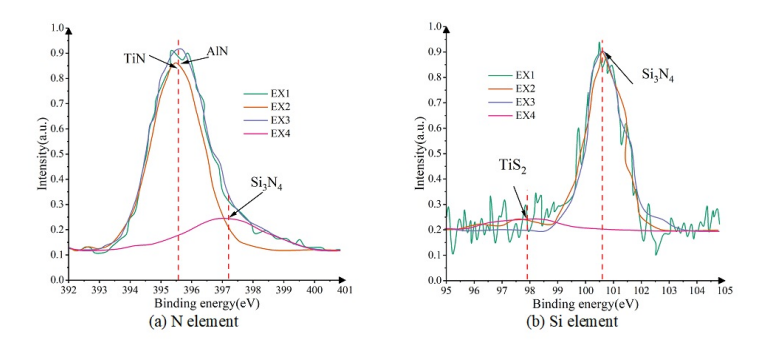


FIGURE 3 XPS spectra of N and Si element in TiSiCN gradient multilayer coating

## 3.2 | Study on mechanical properties of coatings

Figure 4 shows the mechanical property variations of different coatings, where Figure 4(a) and (b) represent the load-displacement curve and hardness (H)/reduced elastic modulus (Er), respectively. The load-displacement curve reveals that the mechanical properties of EX3 differ significantly from the other coatings. This is primarily due to the presence of a higher proportion of TiCN ceramic hardening phases in EX3, which disrupts the amorphous carbon framework within the DLC structure. This fundamentally alters the structural characteristics of the amorphous matrix encapsulating nanocrystals. Analysis of the hardness variation indicates that as the gas flow rate increases, the coating hardness first decreases, then increases, and subsequently decreases again. Combining the above structural analysis reveals that a decrease in TiCN ceramic hard phase content leads to reduced coating hardness. However, as the content of amorphous Si<sub>3</sub>N<sub>4</sub> and sp<sup>3</sup> carbon increases, the coating hardness gradually rises. Ultimately, the continuous decline in TiCN ceramic hard phase content causes the coating hardness to decrease again. Therefore, changes in both the TiCN ceramic hard phase and sp<sup>3</sup> carbon content jointly determine the hardness of the composite coating.

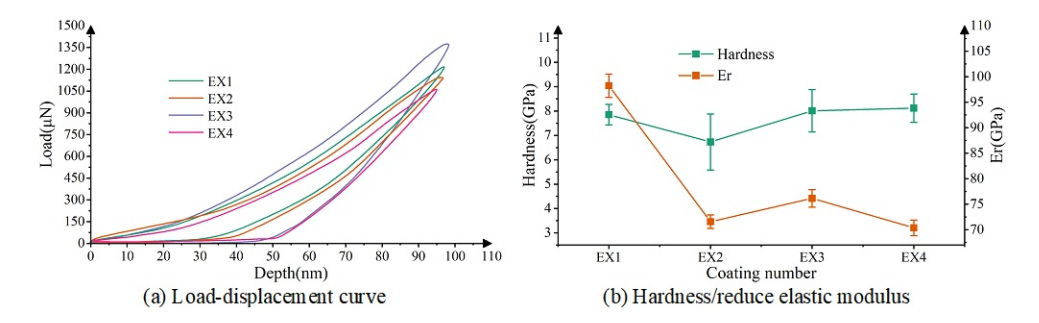


FIGURE 4 The mechanical property variations of different coatings

Table 2 presents the calculated results for H/Er,  $H^3/Er^2$ , and elastic recovery rate of TiSiCN composite coatings under different gas flow rates. H/Er and  $H^3/Er^2$  are typically used to predict coating wear resistance. The elastic recovery rate serves to compare the magnitude of elastic deformation in coatings; a higher recovery rate indicates superior elastic properties of the material. As shown in the table, both  $H^3/Er^2$  and elastic recovery rate first increase and then decrease with rising gas content. Among the coatings, EX3 exhibits the most favorable wear resistance prediction.

TA	BLE	2	H/Er and	$1  { m H}^3 / { m Er}^2$	calculation	results

Example	H/Er	$\mathrm{H^3/Er^2}$	Recover rate
EX1	0.09	0.05	0.57
EX2	0.11	0.06	0.63
EX3	0.13	0.12	0.72
EX4	0.08	0.08	0.55

## 3.3 | Friction and wear properties of coatings

Figure 5 shows the friction coefficient curves of the TiSiCN coating with ZrO<sub>2</sub> as the friction partner under different conditions. Figure 5(a) and (b) represent the friction coefficients under open-circuit potential and cathodic protection, respectively.

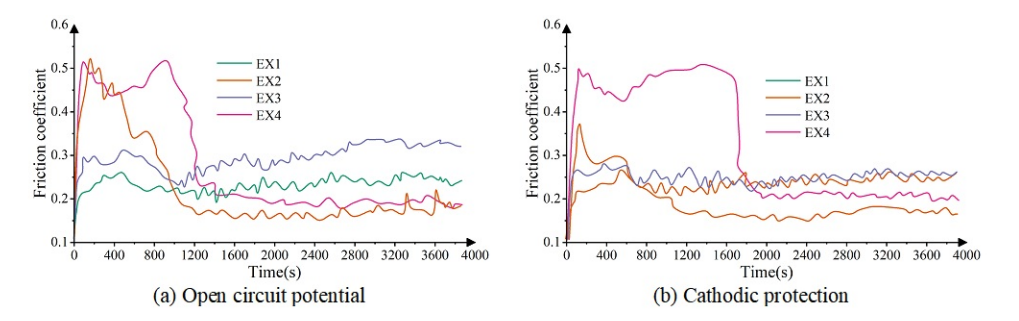


FIGURE 5 Friction coefficient of TiSiCN coating

TABLE 3 The volume loss of the TiSiCN coating

Example	EX1	EX2	EX3	EX4
$T(*10^{-7} mm^{-3})$	3185.36	2665.64	3718.34	3528.13
$W(*10^{-7} mm^{-3})$	3136.04	2651.31	3694.98	3503.06
$W_0(*10^{-7} \text{mm}^{-3})$	3037.28	2174.26	3143.29	3235.57
$W_c(*10^{-7} \text{mm}^{-3})$	93.65	481.35	534.32	253.43
$C(*10^{-7} \text{mm}^{-3})$	51.34	14.42	20.83	17.12
$C_0(*10^{-7} mm^{-3})$	28.73	12.16	18.94	13.58
$C_w(*10^{-7} \text{mm}^{-3})$	23.85	2.27	1.85	3.56
$S(*10^{-7} mm^{-3})$	118.02	482.09	535.06	257.78
S/T	3.71%	18.09%	14.39%	7.31%

Table 3 lists the volume loss of the TiSiCN coating during friction testing. In both cases, the friction coefficient curves can be divided into two stages: the running-in period and the stable period. The transition from an initial unstable state to a stable low-coefficient state may result from the combined effects of the following mechanisms:

First, during friction, carbides within the coating undergo phase transformation to form amorphous carbon, which transfers onto the grinding balls, thereby reducing the TiSiCN coating's friction coefficient. Comparing friction coefficients under different gas flow rates indicates this lubrication mechanism is not dominant. Second, high contact stresses between the coating and friction pair cause continuous exfoliation of sharp-edged abrasive particles at coating scratches. Under alternating stresses, these particles accumulate at scratch sites and

undergo interface polishing. At a certain point, they may transition from sliding friction to rolling friction between the coating and grinding ball, exerting anti-friction effects. Single-layer TiSiCN coatings exhibit the longest running-in time during friction, owing to their highest contact stress and greatest surface roughness. As gas flow increases, surface roughness decreases, progressively reducing the required running-in time for corresponding coatings. Third, the amorphous  $Si_3N_4$  and SiC in the TiSiCN coating react with water during friction to form  $SiO_2$  and  $Si(OH)_4$  colloids. These cover the abrasion marks, providing lubrication and reducing the friction coefficient. At a gas flow ratio of 4:6, the TiSiCN coating exhibits the highest hardness and the lowest friction coefficient.

## 3.4 | Corrosion resistance of coatings

#### 3.4.1 | Corrosion kinetic curve

By measuring the corrosion potential and self-corrosion current density of the coating under different gas flow rates using an electrochemical workstation, the results are shown in Figure 6. As seen in the figure, for the TiSiCN coating at a gas flow ratio of 2:8, the self-corrosion current density and corrosion potential are  $1.652\times10^{-7}$  A/cm<sup>2</sup> and -0.5043 mV, respectively. At a gas flow ratio of 5:5, the self-corrosion current density and corrosion potential were  $2.235\times10^{-7}$  A/cm<sup>2</sup> and -0.4094 mV, respectively. Comparing the self-corrosion potentials of coatings at different ratios reveals that as the gas flow ratio increases, the open-circuit potential generally rises with minor fluctuations within a small range, indicating enhanced corrosion resistance. Notably, when the gas flow ratio increases from 2:8 to 4:6, the self-corrosion potential of the coating shows a significant improvement. After further increasing the ratio to 5:5, the self-corrosion potential of the TiSiCN coating exhibits only minor changes. As the gas flow ratio increases, the self-corrosion current density undergoes a continuous and sustained increase.

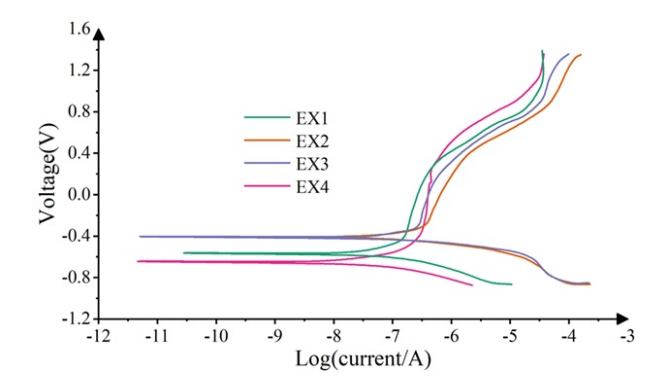


FIGURE 6 Potentiodynamic polarization curve of TiSiCN coating

Regarding changes in the self-corrosion potential of the coating, the influence of gas flow ratio on the coating's corrosion resistance can be analyzed from the following aspects:

(1) Based on the corrosion kinetics curves in the figure, it can be observed that the self-corrosion potential of all curves exceeds -0.9 V. In reality, the standard reduction potential of Ti metal is -1.51 V. The reason its self-corrosion potential significantly increases is that Ti readily passivates in atmospheric environments—its passivation capability even surpasses that of Al—making it highly prone to forming a passivation film. When

anodic current (positive ions) penetrates this passivation film, it encounters substantial resistance, causing its potential to shift markedly toward the positive side.

(2) During electrochemical corrosion, metals undergo oxygen absorption corrosion and hydrogen evolution corrosion at the cathode. Since oxygen possesses stronger electron affinity than hydrogen ions, oxygen absorption corrosion occurs preferentially in any electrolyte solution containing oxygen—regardless of acidity, alkalinity, or neutrality. Oxygen concentration exerts a dual effect on easily passivated metals: it accelerates corrosion while simultaneously inhibiting it through oxygen consumption. Specifically, during oxygen steady-state diffusion, the oxygen absorption corrosion rate is governed by concentration polarization. The coatings with ratios of 2:8 and 4:6 exhibit pronounced concentration polarization in the cathodic polarization region, clearly marking the transition from oxygen absorption corrosion to hydrogen evolution corrosion. This process correlates with the equivalent circuit and impedance magnitude of the coating.

(3) As the ratio continues to increase to 5:5, the coating microstructure shows minimal further changes. However, the increased ratio promotes carbon substitution for nitrogen to form solid solutions or amorphous carbon aggregation, resulting in more amorphous structures. This suppresses the growth trend of TiN columnar crystals, leading to fine, uniform, and dense coating grains. Consequently, the self-corrosion potential exhibits a slight increase.

#### 3.4.2 | AC impedance spectrum curve

To further analyze the corrosion resistance of TiSiCN, a combined analysis of polarization curves and electrochemical impedance spectroscopy (EIS) was conducted. The EIS results in a 4 wt.% NaCl solution are shown in Figure 7, where Figure 7(a) to (c) represent the Nyquist plot and Bode plot, respectively. Since three capacitive arcs are visible in both the Nyquist plot and Bode plot, the EIS data were fitted using an equivalent circuit with three time constants, as illustrated in Figure 7(d).

The Nyquist plot reveals that the EX4 sample exhibits the smallest capacitive arc, indicating the poorest corrosion resistance. This is attributed to the single-layer structure of the TiSiCN coating, whereas the EX1–EX3 samples feature multilayer structures. In the equivalent circuit,  $CPE_f$  and  $R_f$  represent the dielectric properties of the coating, while  $CPE_{dl}$  and  $R_{ct}$  represent the charge transfer process within the double layer.  $R_s$  represents the solution resistance,  $R_{ct}$  represents the charge transfer resistance of the coating,  $R_f$  represents the pore resistance of the coating, while  $CPE_{dl}$  and  $CPE_f$  respectively represent the double-layer capacitance and the coating capacitance. The high degree of agreement between the curve fitted from the equivalent circuit and the EIS curve effectively reflects the electrochemical corrosion behavior of the coating.

Table 4 presents the corresponding fitting results. The polarization resistance  $R_p$  is obtained by summing the solution resistance, the charge transfer resistance of the coating, and the pore resistance of the coating. It relates to the diffusion of electrolytes in the solution through defects in the coating and can be used to predict the coating's corrosion resistance. A higher  $R_p$  value indicates that the coating possesses better corrosion resistance. Calculations yield  $R_p$  values of  $3.488 \times 10^4 \ \Omega \cdot \text{cm}^2$ ,  $3.519 \times 10^4 \ \Omega \cdot \text{cm}^2$ ,  $2.297 \times 10^5 \ \Omega \cdot \text{cm}^2$ , and  $2.633 \times 10^4 \ \Omega \cdot \text{cm}^2$  for the EX1, EX2, EX3, and EX4 coating samples, respectively. Among these, the EX3 coating sample exhibits the highest polarization resistance value, corresponding to its lowest corrosion current density. Conversely, the EX4 coating sample demonstrates the lowest polarization resistance value. Although prepared using the same gas flow rate, it consists solely of a single-layer TiSiCN coating. These results indicate that the gradient structure effectively impedes the corrosion medium from penetrating the substrate material through coating defects, thereby exhibiting outstanding corrosion resistance properties.

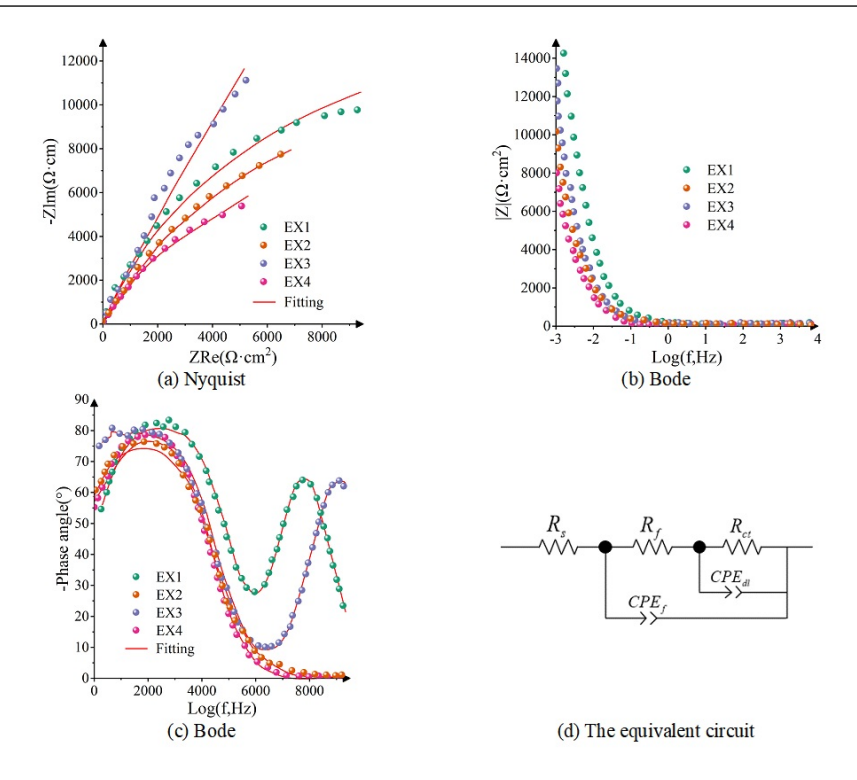


FIGURE 7 EIS results of TiSiCN coatings

TABLE 4 Fitting data of EIS results for the as-deposited coatings

Index	EX1	EX2	EX3	EX4
$R_s(\Omega \cdot cm^2)$	1.463	25.796	1.232	29.541
$CPE_f(\Omega \cdot cm^2)$	$1.207*10^{-5}$	$2.288*10^{-3}$	$2.311*10^{-6}$	$1.054*10^{-3}$
$n_1$	0.903	0.867	0.863	0.852
$R_f(\Omega \cdot cm^2)$	22.15	20691	25.74	23511
$CPE_{dl}(\Omega \cdot cm^2)$	$3.401*10^{-4}$	$1.293*10^{-3}$	$6.768*10^{-4}$	$1.648*10^{-3}$
$n_2$	0.821	0.775	0.782	0.657
$R_{ct}(\Omega \cdot cm^2)$	34852	4763	229658	2789

## 4 | Research findings and application recommendations

## 4.1 | Research findings

To analyze the corrosion resistance of protective coatings in industrial equipment, this study investigates the performance of TiSiCN protective coatings in the cemented carbide tool industry. By preparing TiSiCN coatings

under different gas flow rates, their phase structure, mechanical properties, wear and friction characteristics, and corrosion resistance were verified and analyzed. The study reveals that under identical coating structures (EX1~EX3), increasing carbon content in the TiSiCN coating elevates its corrosion current density while decreasing its polarization resistance. These changes collectively indicate diminished corrosion resistance. Under identical coating compositions, the multilayer TiSiCN (EX3) coating exhibited a reduced corrosion current density compared to the monolayer TiSiCN coating, while its polarization resistance showed a significant increase. This is primarily attributed to the multilayer gradient structure effectively interrupting throughgrowth defects, preventing direct corrosion of the substrate by the corrosive medium, and thereby enhancing the coating's corrosion resistance.

## 4.2 | Application recommendations

- (1) Surface Protection Methods. During industrial equipment operation, when two materials cannot be allowed to come into direct contact yet must be selected, surface protection measures may be adopted based on usage conditions, design requirements, ease of maintenance, and economic principles to prevent direct contact between the two materials. First, utilize the high barrier shielding properties of organic coatings to isolate metal surfaces from electrolytes, physically shielding anodes and cathodes to prevent or slow metal corrosion. Plating involves covering less corrosion-resistant metals with more resistant metals or non-metals, isolating the base metal from corrosive media to achieve corrosion protection. Surface coatings and plating are currently the most economical and widely applied methods for preventing corrosion. Second, isolation protection using sealants and inert materials. Where feasible, sealants and inert materials can be filled between dissimilar materials to create insulation, effectively preventing corrosion.
- (2) The coating process is critical to the quality and effectiveness of protective coatings. The coating process should include surface preparation, application, and curing stages. During surface preparation, pump equipment surfaces must undergo cleaning, rust removal, and degreasing to ensure strong coating adhesion. In the application stage, appropriate methods such as spraying, brushing, or dipping should be selected, with coating thickness and uniformity controlled according to specific process requirements. During curing, suitable methods and conditions—such as natural curing, thermal curing, or UV curing—should be employed to ensure rapid solidification and the formation of a robust protective layer. Furthermore, rigorous quality control and inspection of the coating must be conducted to guarantee excellent corrosion resistance and aesthetic appearance.

#### References

- [1] Qin, J., Chen, Q., Yang, C., & Huang, Y. (2016). Research process on property and application of metal porous materials. *Journal of Alloys and Compounds*, 654, 39-44.
- [2] Lewandowski, J. J., & Seifi, M. (2016). Metal additive manufacturing: a review of mechanical properties. Annual Review of Materials Research, 46(1), 151-186.
- [3] Balamurugan, A., Rajeswari, S., Balossier, G., Rebelo, A. H. S., & Ferreira, J. M. F. (2008). Corrosion aspects of metallic implants—An overview. *Materials and Corrosion*, 59(11), 855-869.
- [4] Aljibori, H. S., Alamiery, A., & Kadhum, A. A. H. (2023). Advances in corrosion protection coatings: A comprehensive review. *International Journal of Corrosion and Scale Inhibition*, 12(4), 1476-1520.

[5] Nazeer, A. A., & Madkour, M. (2018). Potential use of smart coatings for corrosion protection of metals and alloys: A review. *Journal of Molecular Liquids*, 253, 11-22.

- [6] Wang, D., & Bierwagen, G. P. (2009). Sol-gel coatings on metals for corrosion protection. Progress in Organic Coatings, 64(4), 327-338.
- [7] Wang, Y., Yu, H., Chen, C., & Zhao, Z. (2015). Review of the biocompatibility of micro-arc oxidation coated titanium alloys. *Materials & design*, 85, 640-652.
- [8] Qi, X., Li, J., He, Y., Liu, Y., Liu, R., & Song, R. (2023). Study on the wear resistance and corrosion behaviour of self-sealed MAO/ZrO2 coatings prepared on 7075 aluminium alloy. *Journal of Alloys and Compounds*, 969, 172436.
- [9] Chen, F., Zhou, H., Yao, B., Qin, Z., & Zhang, Q. (2007). Corrosion resistance property of the ceramic coating obtained through microarc oxidation on the AZ31 magnesium alloy surfaces. Surface and Coatings Technology, 201(9-11), 4905-4908.
- [10] Wei, T., Yan, F., & Tian, J. (2005). Characterization and wear-and corrosion-resistance of microarc oxidation ceramic coatings on aluminum alloy. *Journal of Alloys and Compounds*, 389(1-2), 169-176.
- [11] Lyon, S. B., Bingham, R., & Mills, D. J. (2017). Advances in corrosion protection by organic coatings: What we know and what we would like to know. Progress in Organic Coatings, 102, 2-7.
- [12] Rout, T. K., Jha, G., Singh, A. K., Bandyopadhyay, N., & Mohanty, O. N. (2003). Development of conducting polyaniline coating: a novel approach to superior corrosion resistance. Surface and Coatings Technology, 167(1), 16-24.
- [13] Ono, S., Tsuge, H., Nishi, Y., & Hirano, S. I. (2004). Improvement of corrosion resistance of metals by an environmentally friendly silica coating method. *Journal of Sol-Gel Science and Technology*, 29(3), 147-153.
- [14] Díaz, I., Chico, B., De La Fuente, D., Simancas, J., Vega, J. M., & Morcillo, M. (2010). Corrosion resistance of new epoxy-siloxane hybrid coatings. A laboratory study. Progress in Organic Coatings, 69(3), 278-286.
- [15] Wang, P., & Cai, D. (2020). Preparation of Graphene-Modified Anticorrosion Coating and Study on Its Corrosion Resistance Mechanism. International Journal of Photoenergy, 2020(1), 8846644.
- [16] Xu, H., & Zhang, Y. (2019). A review on conducting polymers and nanopolymer composite coatings for steel corrosion protection. *Coatings*, 9(12), 807.
- [17] Baghery, P., Farzam, M., Mousavi, A. B., & Hosseini, M. (2010). Ni-TiO2 nanocomposite coating with high resistance to corrosion and wear. Surface and Coatings Technology, 204 (23), 3804-3810.
- [18] Eremin, E. N., Yurov, V. M., Ibatov, M. K., Guchenko, S. A., & Laurynas, V. C. (2016). Anti-corrosion wear-resistant coatings on parts of oil field equipment. *Procedia Engineering*, 152, 594-600.
- [19] Wu, G., Dai, W., Zheng, H., & Wang, A. (2010). Improving wear resistance and corrosion resistance of AZ31 magnesium alloy by DLC/AlN/Al coating. Surface and Coatings Technology, 205(7), 2067-2073.
- [20] Aal, A. A. (2008). Hard and corrosion resistant nanocomposite coating for Al alloy. Materials Science and Engineering: A, 474(1-2), 181-187.
- [21] Li, H., Zhang, C., Liu, C., & Huang, M. (2019). Improvement in corrosion resistance of CrN coatings. Surface and Coatings Technology, 365, 158-163.
- [22] Liu, B., Yan, S., He, Y., He, T., He, Y., Song, R., ... & Li, Z. (2022). Study on wear resistance and corrosion resistance of zirconium phenylphosphonate reinforced Ni–W composite coating. Applied Surface Science, 603, 154483.

[23] Li, Y., & Shi, Y. (2021). Microhardness, wear resistance, and corrosion resistance of AlxCrFeCoNiCu high-entropy alloy coatings on aluminum by laser cladding. Optics & Laser Technology, 134, 106632.

- [24] Hosking, N. C., Ström, M. A., Shipway, P. H., & Rudd, C. D. (2007). Corrosion resistance of zinc-magnesium coated steel. Corrosion Science, 49(9), 3669-3695.
- [25] Amadi, S. A., & Ukpaka, C. P. (2014). Performance evaluation of anti-corrosion coating in an oil industry. International Journal of Novel Research in Engineering & Pharmaceutical Science, 1 (03), 41-49.
- [26] Brito, V. S., Bastos, I. N., & Costa, H. R. M. (2012). Corrosion resistance and characterization of metallic coatings deposited by thermal spray on carbon steel. *Materials & Design*, 41, 282-288.
- [27] Ates, M. (2016). A review on conducting polymer coatings for corrosion protection. Journal of Adhesion Science and Technology, 30 (14), 1510-1536.
- [28] Fenker, M., Balzer, M., & Kappl, H. (2014). Corrosion protection with hard coatings on steel: Past approaches and current research efforts. Surface and Coatings Technology, 257, 182-205.
- [29] Qian, Y., Li, Y., Jungwirth, S., Seely, N., Fang, Y., & Shi, X. (2015). The application of anti-corrosion coating for preserving the value of equipment asset in chloride-laden environments: a review. *International Journal of Electrochemical Science*, 10(12), 10756-10780.
- [30] Kadhim, M. G., & Ali, M. T. (2017). A critical review on corrosion and its prevention in the oilfield equipment. Journal of Petroleum Research and Studies, 7(2), 162-189.
- [31] Tillmann, W., Urbanczyk, J., Thewes, A., Braeuer, G., & Dias, N. F. L. (2024). Effect of the TiSiN interlayer properties on the adhesion and mechanical properties of multilayered TiSiCN thin films. Surface and Coatings Technology, 478, 130467.
- [32] Menshakov, A. I., & Bryuhanova, Y. A. (2024). Tribomechanical Properties of TiSiCN Coatings Obtained by Anodic Evaporation of Titanium and Decomposition of Hexamethyldisilazane in a Discharge in a System with a Self-Heating Hollow Cathode. *Journal of Surface Investigation: X-ray, Synchrotron and Neutron Techniques*, 18(5), 1265-1270.
- [33] Baimoldanova, L., Rakhadilov, B., Kengesbekov, A., & Kuanyshbai, R. (2024). Influence of mechanical activation on the evolution of TiSiCN powders for reactive plasma spraying. Crystals, 14(11), 1005.
- [34] Ortiz, C. H., Hernandez-Renjifo, E., & Caicedo, J. C. (2024). Evaluation of the tribological behavior of TiSiCN (a-SiCN/nc-TiSiCN) nanocomposite coatings. *Materials Chemistry and Physics*, 317, 129095.